energies

MDPI

Article

Synthesis of V_2O_5/Single-Walled Carbon Nanotubes Integrated into Nanostructured Composites as Cathode Materials in High Performance Lithium-Ion Batteries

Nojan Aliahmad [1,†], Pias Kumar Biswas [1,2,†], Hamid Dalir [1,2,*] and Mangilal Agarwal [1,2,*]

1 Integrated Nanosystems Development Institute (INDI), Indiana University-Purdue University Indianapolis, Indianapolis, IN 46202, USA; nojan@iu.edu (N.A.); piasbisw@iu.edu (P.K.B.)
2 Department of Mechanical and Energy Engineering, Indiana University-Purdue University Indianapolis, Indianapolis, IN 46202, USA
* Correspondence: hdalir@iu.edu (H.D.); agarwal@iupui.edu (M.A.)
† These authors contributed equally to this work.

Abstract: Vanadium pentoxide (V_2O_5)-anchored single-walled carbon nanotube (SWCNT) composites have been developed through a simple sol–gel process, followed by hydrothermal treatment. The resulting material is suitable for use in flexible ultra-high capacity electrode applications for lithium-ion batteries. The unique combination of V_2O_5 with 0.2 wt.% of SWCNT offers a highly conductive three-dimensional network. This ultimately alleviates the low lithium-ion intercalation seen in V_2O_5 itself and facilitates vanadium redox reactions. The integration of SWCNTs into the layered structure of V_2O_5 leads to a high specific capacity of 390 $mAhg^{-1}$ at 0.1 C between 1.8 to 3.8 V, which is close to the theoretical capacity of V_2O_5 (443 $mAhg^{-1}$). In recent research, most of the V_2O_5 with carbonaceous materials shows higher specific capacity but limited cyclability and poor rate capability. In this work, good cyclability with only 0.3% per cycle degradation during 200 cycles and enhanced rate capability of 178 $mAhg^{-1}$ at 10 C have been achieved. The excellent electrochemical kinetics during lithiation/delithiation is attributed to the chemical interaction of SWCNTs entrapped between layers of the V_2O_5 nanostructured network. Proper dispersion of SWCNTs into the V_2O_5 structure, and its resulting effects, have been validated by SEM, TEM, XPS, XRD, and electrical resistivity measurements. This innovative hybrid material offers a new direction for the large-scale production of high-performance cathode materials for advanced flexible and structural battery applications.

Keywords: vanadium pentoxide; carbon nanotubes; lithium-ion batteries; nanocomposite materials; xerogel; hybrid cathodes

check for updates

Citation: Aliahmad, N.; Biswas, P.K.; Dalir, H.; Agarwal, M. Synthesis of V_2O_5/Single-Walled Carbon Nanotubes Integrated into Nanostructured Composites as Cathode Materials in High Performance Lithium-Ion Batteries. *Energies* **2022**, *15*, 552. https://doi.org/10.3390/en15020552

Academic Editor: Cai Shen

Received: 14 December 2021
Accepted: 11 January 2022
Published: 13 January 2022

Publisher's Note: MDPI stays neutral with regard to jurisdictional claims in published maps and institutional affiliations.

Copyright: © 2022 by the authors. Licensee MDPI, Basel, Switzerland. This article is an open access article distributed under the terms and conditions of the Creative Commons Attribution (CC BY) license (https://creativecommons.org/licenses/by/4.0/).

1. Introduction

Over the past decade, lithium-ion batteries have been significantly improved to achieve higher capacities and life cycle. However, advancements in electronic devices have also increased the necessity of developing thin lithium-ion batteries with flexible properties [1]. Recently, there has been a shift in research toward utilizing advanced materials to create new battery technologies that are not only safer, cheaper, and more durable [2,3], but that are also lightweight, thin, and flexible [4–6]. More recently, high current density materials have been explored, synthesized, and produced in an attempt to achieve even lighter, more compact batteries with increased current output. Increasing the active surface area of electrodes is a key strategy to provide higher material-recurrent densities. Here, the use of nanomaterials to create uniform 2D or 3D structures can effectively increase surface area and provide a higher current/capacity for lithium-ion batteries [7–9]. Further, these structures improve lithium nesting and increase the reversibility of resulting battery cells [10,11].

Three-dimensional crystals that have been developed using spinel lithium manganese oxide (a common cathode material that is known to be reliable and robust) can enable higher lithium diffusion and better cycle life than 2D ones. However, the capacity of these materials proved to be slightly lower than 2D crystals [12]. Other 3D materials based on phosphates have also been created, and while recent work shows these materials could be a promising solution to achieve higher capacities, they are still in the research phase to mitigate some challenges, including high processing cost, low cycle life, etc. [13,14]. Other metal oxide 3D materials, including LNMC ($LiNi_{1/3}Mn_{1/3}Co_{1/3}O_2$) (164.4 $mAhg^{-1}$) [15], lithium iron phosphate ($LiFePO_4$) (170 $mAhg^{-1}$) [16], and lithium manganese oxide ($LiMn_2O_4$) (117 $mAhg^{-1}$) [16] have also been developed to achieve high and ultra-high specific capacities. The LNMC alloy (in spherical shape) can be used as a lithium nest to produce capacities in the range of 164.4 $mAhg^{-1}$ and voltages in the range of 2.8 to 4.3 V. This is a suitable material for high voltage applications, but its capacity is only moderate [17]. In addition, material synthesis costs are higher compared to conventional lithium salts. $LiFePO_4$ suffers from similar characteristics, with a capacity limited to 170 $mAhg^{-1}$ (although this is still 20–25% higher than conventional lithium salts). While this material has good durability, its voltage plateau is limited to 3.4 volts. $LiMn_2O_4$ represents another active material for lithium-ion batteries. This material takes the form of nano spinels and crystals, which can provide capacities up to 150 $mAhg^{-1}$ and high voltages in the range of 3.5–4.3 volts. In spinel form, the capacity fade is also limited such that it can be cycled up to 200 times. In contrast to the other materials, fabrication is far easier. The one limiting factor is its sensitivity to high C rate charge–discharge cycles. Here, the voltage plateau of the cell drops, and the capacity becomes lower by 30%, which inhibits its use in high current applications or with fast charge. Moreover, the theoretical capacities for these materials are still only 10% to 20% higher than commercially available lithium-ion batteries.

While the above materials can provide the desired cyclability and high energy density for flexible lithium-ion batteries, their theoretical capacity is still not adequate to meet the needs of new-age wearable and flexible electronic devices and high-power applications. In order to reach a higher specific capacity/energy, new ultra-high capacity electrode materials are required. In this paper, vanadium pentoxides have been investigated owing to their multi-valence transition throughout the charging–discharging phase, which provides high capacities [18]. Furthermore, vanadium is accessible, low cost, and abundant in nature and can also be synthesized in lab scale [19,20]. Through a simple fabrication processes, the sol–gel of this material can be utilized as an active cathode material for high performance lithium-ion batteries, as it produces a 3D crystal structure that offers nests for lithium ions [21]. Due to the intercalation of lithium atoms into the gaps between the layers of VO_5 octahedra, the insertion of lithium atoms into V_2O_5 causes the phase transition of V_2O_5 to $Li_xV_2O_5$, causing deformation of the layered structure (Figure 1a,b) [22]. During lithiation, the deformed pyramid structure of pristine V_2O_5 can be retained, but the smooth layers of pristine V_2O_5 will pucker more as the insertion number x increases [23]. The chemical structure of V_2O_5 is shown in Figure 1a [24,25], and the crystalline structure from (100) facet of lithiated $Li_xV_2O_5$ ($1 < x < 3$) is shown in Figure 1b.

V_2O_5 can intercalate with three lithium ions to provide a theoretical capacity of 443 $mAhg^{-1}$ and specific energy of 1550 $Whkg^{-1}$. The major issues that hamper it in attaining the theoretical specific capacity or higher energy density by V_2O_5 in practical lithium-ion battery applications are low electron conductivity of the V_2O_5 nanoribbons, slow diffusion rate, and irreversible phase transitions upon deep discharge [26–29]. To overcome these challenges, conductive materials such as graphene, copper and carbon nanotubes (CNTs) have been incorporated into the V_2O_5 structure using direct mixing [30,31] or via gel formation [32]. These carbon-based materials are not only capable of increasing conductivity in electrode structures but are also improving mechanical stability [33]. SWCNT has superior properties compared with graphene or copper with respect to high conductivity, mechanical reliability, and thermal stability. Furthermore, SWCNT has unique electrical characteristics due to its distinct structure [34]. However, for V_2O_5, the direct

mixing of CNT or graphene is not effective due to the lack of particle connections in the atomic layer [35,36]. Moreover, physical mixing of CNT or graphene may hinder electrolyte exposure to the pores and active layer of the active materials. Previously, a method was developed to make graphene-modified V_2O_5 nanostructured cathode materials where the graphene was added in the form of graphene oxide and then reduced to graphene. However, this strategy leads to a non-uniform formation of graphene and partial damages in structure [33]. Therefore, different carbon compounds that are easy to fabricate, more stable, water soluble and conductive are of critical need. Instead of using pre-synthesized V_2O_5 or directly mixed V_2O_5 with carbon-based nanomaterials, here, V_2O_5 is formulated through a simple sol–gel process from $NaVO_3$, and SWCNTs is added before the formation of V_2O_5 such that a V_2O_5 nanoribbon is grown onto the surface of SWCNTs. Thus, highly conductive 3D V_2O_5/SWCNTs network is generated, which elevates the electrochemical performance by eliminating low cyclability and poor rate capability challenges of pristine V_2O_5 and other V_2O_5-carbon based nanomaterial composites.

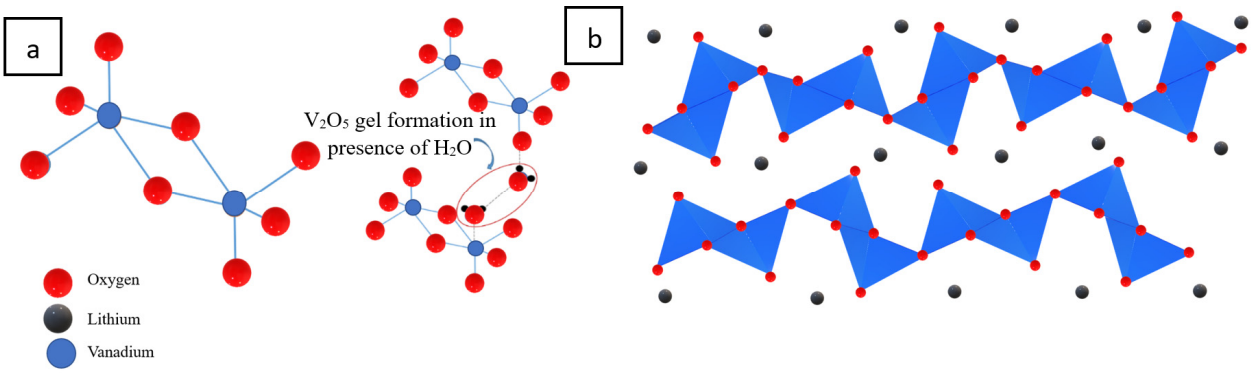

Figure 1. (**a**) Vanadium pentoxide (V_2O_5) chemical structure during gel formation and (**b**) the crystalline structure of lithiated $Li_xV_2O_5$.

In this research, a V_2O_5 xerogel containing SWCNTs was produced in a facile synthesis method to be used as an ultra-high capacity lithium-ion active cathode material. Previously reported V_2O_5 materials have suffered for low-cycle life, but the use of a xerogel represented a solution to create high-capacity and high-coulombic efficiency [29]. In addition, the presence of a small amount of SWCNTs improved both electrical conductivity and cycle life of the resulting material, making it suitable for flexible and non-flexible battery applications in electronic appliances and structural battery applications in automobile industries [37,38].

2. Materials and Methodology

2.1. Materials

Sodium metavanadate ($NaVO_3$), poly(styrenesulfonate) (PSS), n-methyl-2-pyrrolidone (NMP), lithium phosphorous fluoride ($LiPF_6$), ethylene carbonate (EC) and diethyl carbonate (DEC) were purchased from Sigma-Aldrich (St. Louis, MO, USA). SWCNTs and TIMCAL carbon black were purchased from Fisher Scientific. Kynar polyvinylidene fluoride (PVDF) was purchased from Arkema Industries (King of Prussia, PA, USA), Celgard 2400 film was purchased from Celgard (Charlotte, NC, USA), and the proton exchange resin (Dowex-50-WX2, 50–100 mesh) was purchased from Fisher Scientific.

2.2. Synthesis of V_2O_5 Xerogel

The vanadium pentoxide (V_2O_5) xerogel was synthesized using a sol–gel process [39] where 0.1 mol $NaVO_3$ aqueous solution was transferred all through a proton exchange resin. In this process, the gel forms by removal of sodium atoms from the salt, and decavanadic acid (HVO_3) is collected and aged in a centrifuge tube for 3–4 weeks. After this time, the solution's color changes from light yellow to dark red. This color change indicates the

complete formation of vanadium oxide hydrogel, which is later freeze-dried under vacuum to produce a V_2O_5 xerogel.

2.3. Synthesis of SWCNT Solution

A 0.5 mg/mL SWCNT solution was made with poly(styrenesulfonate) (PSS) in a 1:2 ratio, diluting with DI water. The SWCNT solution was then ultrasonicated in a bath sonicator for 24 h in room temperature. This was followed with probe sonication and centrifugation to create the well dispersed CNT solution. A case study was run to check the sustainability of the resulting SWCNT dispersion in water. Here, two parallel solutions of SWCNT: PSS in DI water and SWCNT solution in DI water, were prepared. This is critical, as CNTs need to be well dispersed for a long period, throughout the V_2O_5 formation process. The homogeneous SWCNT: PSS solution remained intact even after two weeks while pure SWCNT precipitated out of the DI solution. Zetasizer (Zetasizer Nano ZSP, Malvern Polytechnical, UK) has been run for both samples (two weeks old), where the z-average size for CNT: PSS solution was found ~600 nm and for CNT solution ~900 nm (Figure S1 of Supplementary Material data). The graphs demonstrate that SWCNTs are well dispersed in the presence of PSS for a longer period than without PSS, and with almost uniform size.

2.4. Synthesis of V_2O_5-SWCNT Integrated Nanostructured Composite

The V_2O_5-SWCNT composite was developed by adding SWCNT: PSS solution to the V_2O_5 xerogel, which was then in HVO_3 form and was allowed to rest for 3–4 weeks in order to produce a uniform V_2O_5-SWCNT hybrid structure. After, the xerogel was freeze-dried to remove excess water. This was followed by pyrolysis at high temperature (400 °C) for 4 h in the air with a heating rate of 10 °C/min. An illustration of the synthesis and resulting structure of the V_2O_5-SWCNTs composite is shown in Figure 2.

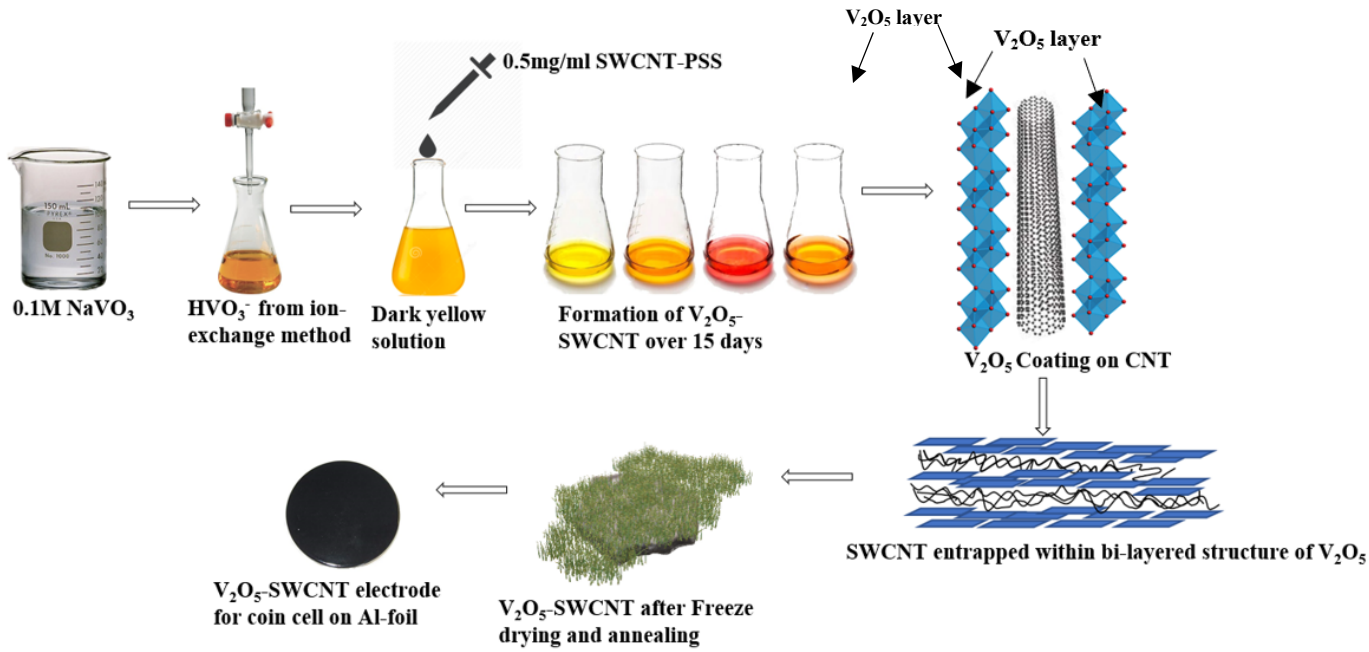

Figure 2. Schematic illustration of the synthesis and structure for the V_2O_5-SWCNTs composite. A 0.1 M solution of sodium metavanadate ($NaVO_3$) is passed through a proton-exchange filter column, and a yellow-colored HVO_3^- solution is obtained. This solution is then mixed with a SWCNT: PSS solution. This mixture slowly forms a V_2O_5 xerogel, with the solution gradually shifting in color from yellow to dark red, marking the complete evolution of a 3D homogeneous network of V_2O_5-SWCNT hydrogel.

2.5. Materials Characterization

The composition and morphology of the electrodes made with the V_2O_5-SWCNT composites were analyzed through electron microscopy, X-ray characterization, and thermogravimetric analysis. Field emission scanning electron microscope (FESEM, JEOL 7800f, Tokyo, Japan) images were acquired at 5 kV, and images using a transmission electron microscope (TEM, Tecnai G2 12 Bio Twin. FEI, Hillsboro, OR, USA) equipped with an AMT CCD camera (Advanced Microscopy Techniques, Danvers, MA, USA) were taken at 80 kV. X-Ray diffraction (XRD, Bruker D8 Discover, USA) patterns of pristine V_2O_5 and V_2O_5-SWCNT were obtained with a 2θ scanning range from 0° to 80°. To analyze the structural change of V_2O_5-SWCNT composite materials at different temperatures, thermogravimetric analysis (TGA) was carried out (TA Instruments SDT-Q600, New Castle, DE, USA) up to 600 °C in the presence of N_2 gas at a heating rate of 10 °C min^{-1}. X-ray photoelectron spectroscopy (XPS, PHI Versaprobe II XPS, Tokyo, Japan) was also performed.

2.6. Electrochemical Characterization

To make the electrodes, as produced V_2O_5/SWCNT (70 wt.%), conductive TIMCAL carbon black (20 wt.%), and PVDF (10 wt.%) were ground and mixed together with NMP and the mixture was allowed to stir overnight at 800 rpm. The resulting solution was then sprayed over a metallic current collector (Al foil) to produce the electrodes. The active material mass loading for vanadium-based electrodes (V_2O_5/CNT) is 0.4 mg/cm^2. The active materials coated on the Al foil was kept in a 90 º C vacuum oven for drying overnight and later calendaring was performed by pressure controlled electric rolling machine (MR-100A, MTI Corporation, Richmond, CA, USA), as this has a direct impact on pore structure and can enhance energy density, and minimize deformability [40]. All electrodes were stored in an argon-filled glovebox. Coin cells having electrode geometric area of 2 cm^2 and cell capacity of 0.8 mAh were fabricated applying a half-cell configuration with lithium foil and V_2O_5/SWCNT electrodes. A Celgard 2400 film was used for separators, with 50 µL of $LiPF_6$ aqueous electrolyte. The electrolyte was a 1.0 M $LiPF_6$ solution in an EC/DEC mixture (1:1 *v/v*). After fabricating the coin cells, they were rested for 12 h to obtain a stable state for analysis. The coin cells were then examined by an Arbin BT2000 battery testing system using different C rates between 1.8 to 3.8 V. AC impedance of the prepared cells was measured with a 1470E Multistat-Solartron Analytic system in the frequency range of 0.01 Hz–1 MHz and with an amplitude of 5 mV.

3. Formation Mechanism of V_2O_5 Xerogel and V_2O_5-SWCNTs Composite

The V_2O_5 xerogel formation mechanism plays a vital role by entrapping SWCNTs in its bilayered structure. As illustrated in Figure 2, $NaVO_3$ transforms into yellow-colored decavanadic acid (HVO_3^-) when eluted through a column exchange resin. After some time (a few minutes), V_2O_5 hydrogel formation starts through the protonation of decavanadic acid [41]. The gel formation continues and after two weeks is dark red-colored, and a 3D-structured ribbon-shaped V_2O_5 hydrogel is formed [25,42]. V_2O_5 nanoribbons are mostly linear, 100–120 nm in length with variable width. When SWCNT is added right after collecting ionic decavanadic acid from the resin exchange column, the V_2O_5 nanoribbon starts formation on the surface of CNTs (as illustrated in Figure 2 and supported by Dr. Xie's group's previous work in [25]). Their sheet-like structure and adherence is attributed to coulombic interactions and van der Waals forces, which is verified in the material characterization section. While the gel making process needs the uniform formation of V_2O_5 nanoribbons around SWCNT, a well-dispersed solution is needed. Making a homogeneous suspension of SWCNTs has been a major challenge due to several solubility parameters and the need to better understand the nanotube-solvent interactions [43]. The dispersion and phase behavior of SWCNT in organic/inorganic solvents is more complex than other anisotropic nanomaterials due to its broad distribution of length, electronic properties, and strong van der Waals intermolecular forces [44]. Well-dispersed SWCNT can be achieved through sidewall functionalization [45] and stabilization by acids containing

hydrophobic groups. Yet, these techniques disrupt the electronic properties of SWCNTs and introduce interferents into the final product. To achieve a stable SWCNT aqueous solution, water-soluble Poly(styrenesulfonate) (PSS) was used, an effective dispersant that does not affect the electrochemical properties of SWCNTs [46,47]. The effect of using PSS in a SWCNT solution has been characterized and is shown in the supplementary data section.

4. Morphology and Structural Characterization

The formation of V_2O_5 is further confirmed by X-ray photoelectron spectroscopy. Figure 3a shows the full spectrum of binding energies with the peaks of vanadium, oxygen, and carbon along with peaks corresponding to silicon that arise from the conductive silicon wafer used for sample mounting. Figure 3b shows the V2p spectrum with the specific binding energy for $V_{2p1/2}$ (521.47 eV) and $V_{2p3/2}$ (514.21 eV), which is consistent with those of V^{5+} in V_2O_5 [48]. Here, the center peaks of $V_{2p1/2}$ and $V_{2p3/2}$ are slightly shifted to lower binding energies due to the close affinity of V_2O_5 to SWCNT [49]. The C1s could be deconvoluted into three peaks, implying the presence of carbon atoms in three types of chemical surroundings [50]. The prime peak at 281.70 eV from sp^2-hybridized carbon atoms of the graphene sheets shifts to the left by 2.9 eV due to the interaction between V_2O_5 and SWCNT [51]. The intermediate peak at 283.15 eV is attributed to single-coordinated C–O bonds in carboxyl groups and the lowest peak, 286.2 eV, corresponds to the smallest carbonyl (C=O) groups. Figure 3d shows two asymmetrical O1s peaks matching with the principal peak corresponding to O atoms in V_2O_5 and -OH groups peak in higher binding energy. The major peak at 529.7 eV is assigned to oxygen in V_2O_5, while the other peak at 531.6 eV is attributed to hydroxyl groups (-OH), which is consistent with the C1s peak for carboxyl groups [52]. Here, the presence of small functional groups such as hydroxyl (-OH) groups and the peak shifting to the lower binding-energy field further indicate that the nanoparticles of V_2O_5 might be properly associating with the SWCNT surfaces, either via V–O–C or van der Waals forces [49].

The nanostructure and morphology of the V_2O_5–SWCNT composites after freeze drying were characterized by FESEM. Figure 4a exhibits an interconnected, crosslinked, porous framework with numerous uninterrupted nanopores. Conversely, the wall of the structure has several interlocked 2D nanosheets. As seen in Figure 4b, the thickness of such nanosheets is about 100–120 nm. High magnification FESEM images reveal that nanosheets with porous and rugged surfaces are interlinked by ample SWCNTs and V_2O_5 particles in an ordered arrangement. In this case, by introduction of SWCNT in the gel formation phase, a uniform aggregation of CNT fibers has been developed in between V_2O_5 crystals providing electric conductive pathways. This can improve the capacity of the V_2O_5 by increasing the overall electric conductivity of the active material. Better electric conductivity can improve the reversible lithium deposition in crystals. The BET (Brunauer, Emmett and Teller) surface area analysis is used to measure the surface area of pristine V_2O_5 and V_2O_5/SWCNT nanocomposite. The surface areas of 29 and 37 m^2g^{-1} were found for pristine V_2O_5 and V_2O_5-SWCNT nanocomposites, respectively, with irregular pore size featuring in the range of ~3–6 nm in diameter. The relatively higher specific surface area value of the V_2O_5/SWCNT composite is attributed to the presence of SWCNT [49].

TEM was used to investigate the uniform coating of V_2O_5 over SWCNTs and the 2D porous sheet-like structure of V_2O_5-SWCNT composites in the xerogel condition (SEM was used for freeze-dried samples). Here, TEM images verify the sandwiched structure of bilayered V_2O_5 and entrapped SWCNT. This implies the uniform formation of carbon nanotubes around the V_2O_5 sheets. As it was reported by Xie's group [25], in the sol–gel process, V_2O_5 2D crystals can form around the diluted particles in a solution phase. Here, by introduction of carbon nanotubes in the gel formation state, conductive paths have been embedded in between crystals and were identified by TEM as well. The lower magnification image in Figure 5a shows that the composite forms a uniform thick reticulum-shaped network with V_2O_5 agglomerated on the CNT surface. Comparatively, higher magnification images in Figure 5b, and c confirm the porous sheet-like structure of the

V_2O_5-SWCNT hybrid, where both materials are standing side by side, making a cross link. The overall thickness of V_2O_5 layers over SWCNT was measured at many different positions and consistently ranges between 4–10 nm. From the highest magnification image (Figure 5d), a sandwich-like structure was identified, where V_2O_5 and CNTs overlap with each other, forming a repeated structure indicating the homogenous dispersion of SWCNTs into V_2O_5 layers.

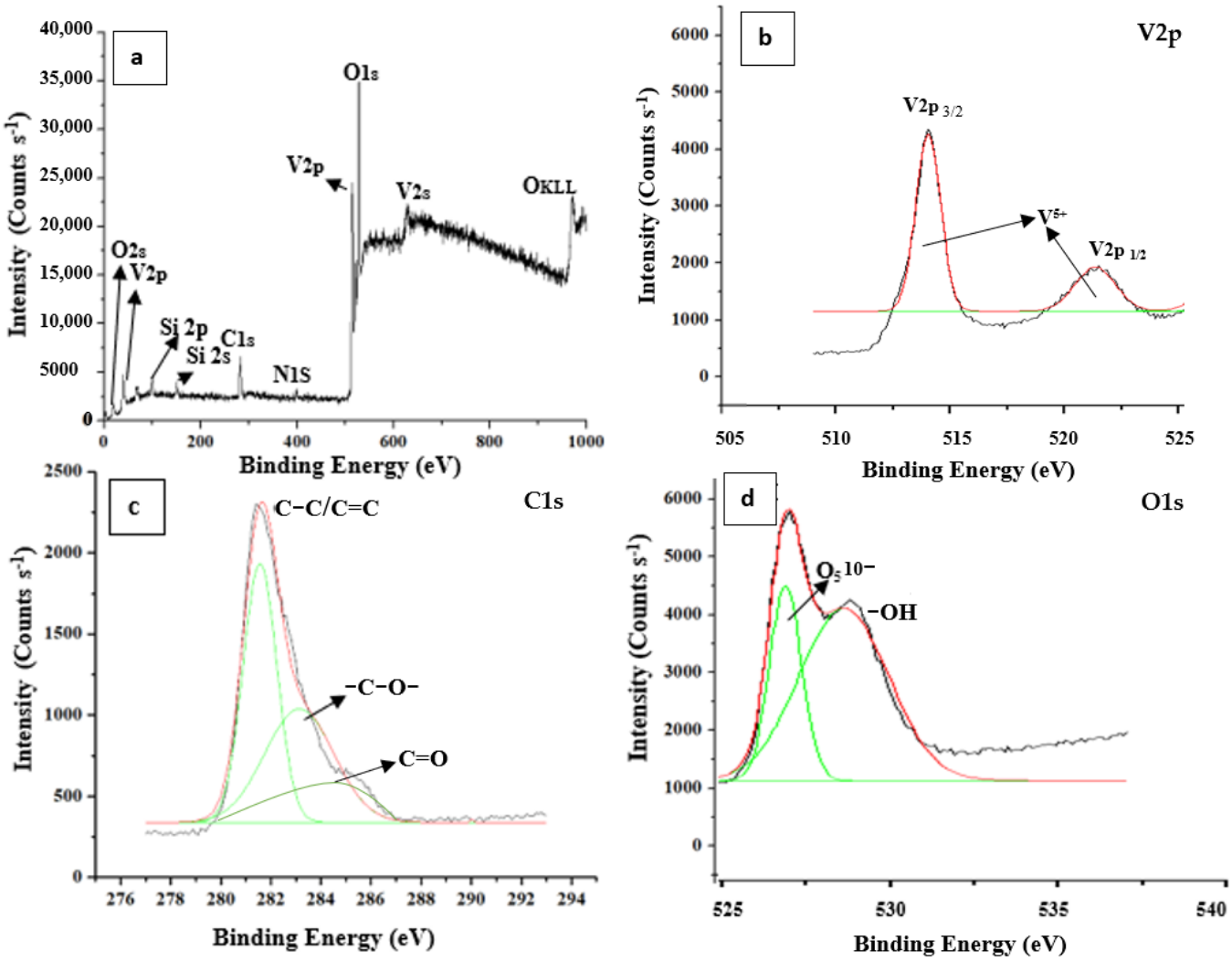

Figure 3. The interaction among SWCNT and V_2O_5 nanoparticles was scrutinized by XPS data shown here. (**a**) Spectrum sample scanning with all elements of carbon, oxygen and vanadium. (**b**) V2p region with 2p3/2 and 2p1/2 orbit splitting showing V^{5+} state. (**c**) C1s region deconvoluted to peaks, suggesting graphitic composition of SWNTs. (**d**) Asymmetrical O1s peak of XPS spectrum fitted with the predominant peak corresponding to O atoms in V_2O_5 and the peak of hydroxyl groups in higher binding energy.

TGA was performed for pristine V_2O_5 and the V_2O_5-SWCNT composites to study structural change and thermal stability during the annealing process. The pristine V_2O_5 shows a speedy weight reduction up to 80 °C (around 0.15%/C) but shows steady weight reduction at a comparatively slower rate (0.020%/C) until it reaches 350 °C. This phenomenon is ascribed to the reduction of H_2O molecules with weak bonding in the V_2O_5 xerogel [53]. When the temperature rises above 350 °C, the closely bonded crystallized H_2O molecules are extracted, and the disordered layer phase starts transforming into the orthorhombic phase [54]. Compared to pristine V_2O_5, V_2O_5/SWNTs shows a different path of weight loss; it shows a gradual weight reduction up to 280 °C (around 0.025%/C) due to

the loss of weakly bonded water in V_2O_5/SWNTs. Later, it shows a slightly faster weight reduction rate (0.060%/C) until it reaches 450 °C. When it comes to the crystal structure, the bi-pyramid configuration can remain stable up to 450 °C in the crystal state, although there are signs indicating the formation of the orthorhombic V_2O_5 structure directly after 400 °C [25]. The aforementioned results also demonstrate the existence of CNT network in the V_2O_5 structure enhances thermal stability significantly. These results are shown in Figure 6.

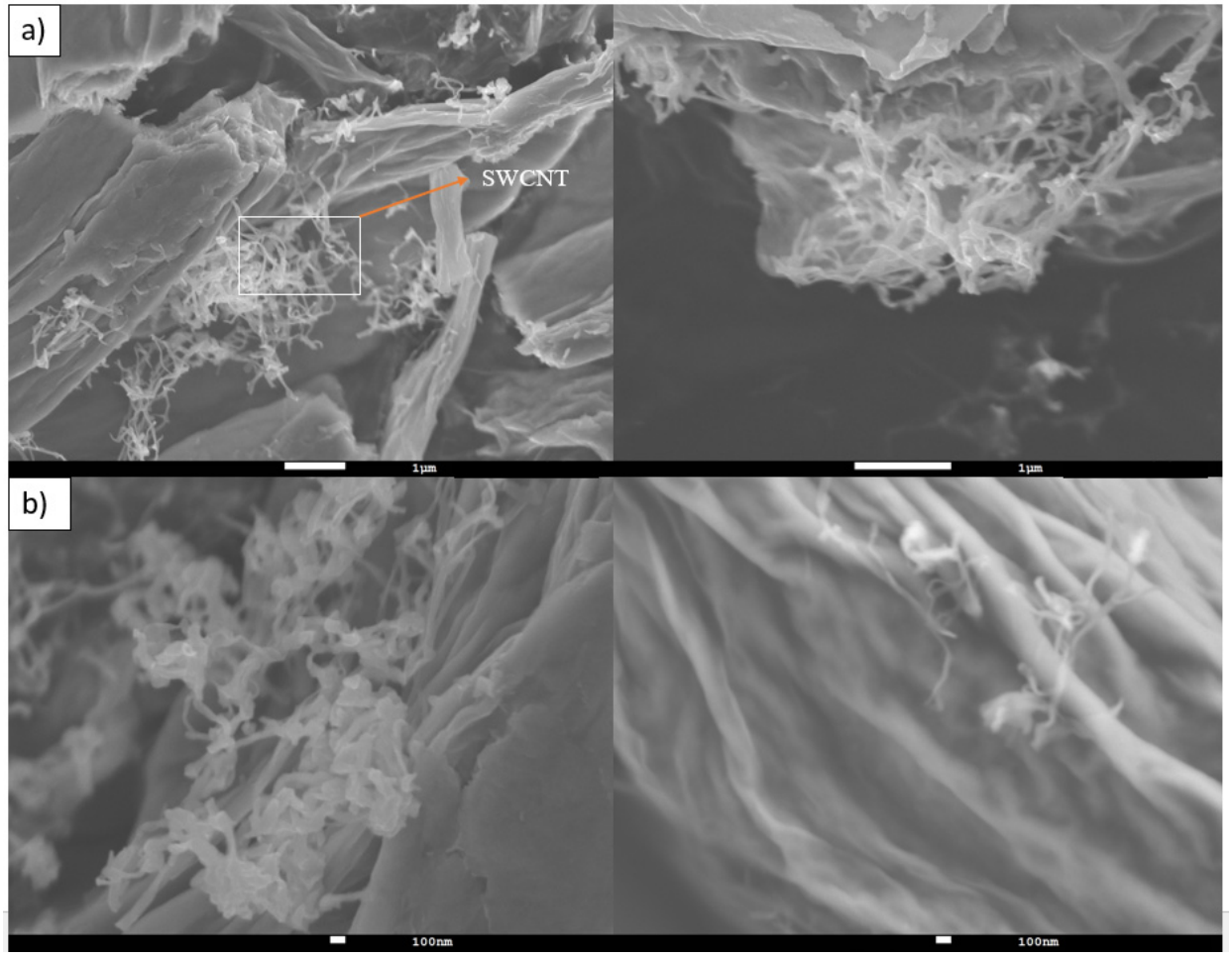

Figure 4. (**a**) The interconnected porous framework of the V_2O_5–SWCNT composite materials contains continuous nanopores. (**b**) Porous and rough sheets create a sandwich-like structure with SWCNTs and V_2O_5 particles.

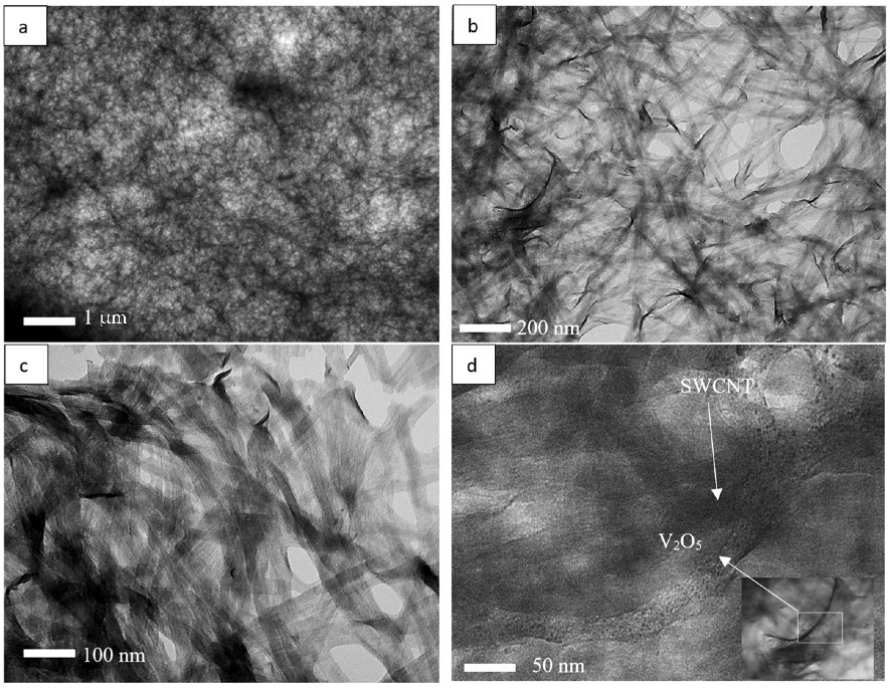

Figure 5. TEM images of the V_2O_5-SWCNT hybrid structure. (**a**) Low magnification TEM images show a network of V_2O_5-SWCNT. (**b**) Higher magnification reveals nanostructures that show parallel strands of SWCNT and V_2O_5 layers. (**c**,**d**) Confirmation that V_2O_5 nanoribbons are sandwiched between SWCNTs with a repeated structure.

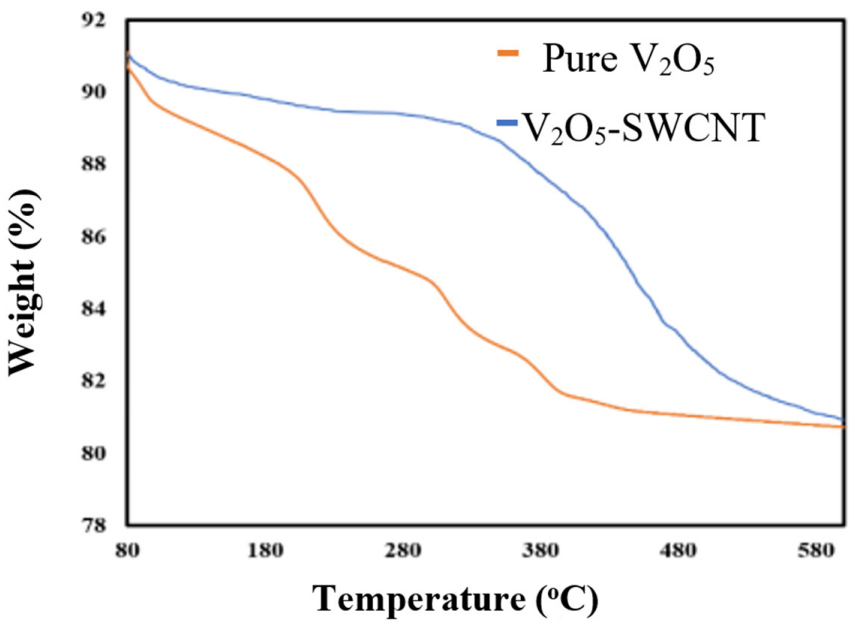

Figure 6. TGA graphs of pristine V_2O_5 and V_2O_5-SWCNT composites showing structural change and thermal stability during the annealing process.

5. Results and Discussion

Systematic assessments were performed in a voltage range of 1.8–3.8 V to compare the electrochemical output of hybrid V_2O_5-SWCNT and pure V_2O_5. As shown in Figure 7a,b, pure V_2O_5 shows 175 mAhg^{-1}, which computes to 40% of theoretical capacity. By contrast, V_2O_5 with 0.2% wt. SWCNTs shows far superior specific capacity of 390 mAhg^{-1}, around 88% of the theoretical capacity of V_2O_5, which is 443 mAhg^{-1}. This high capacity suggests that almost all three Li^+ ions participated in the lithiation and de-lithiation process for each

V_2O_5 molecule of the V_2O_5-SWCNT composite. The voltage profile reveals that inserted Li^+ ions are removed during charge/discharge, which helps to gain good reversibility for V_2O_5-SWCNT cathode materials. Some capacity loss was observed gradually but has been attributed to the irreversible delithiation at deep discharge conditions, as some Li^+ ions must have permanently inserted into the V_2O_5 matrix and could not be extracted as shown in Figure 7c,d. The V_2O_5-SWCNT composite shows high specific capacity (250 $mAhg^{-1}$) even at a high rate (1 C), which is 2.27 times more than pure V_2O_5 (110 $mAhg^{-1}$). The coulombic efficiency of 100 cycles with high rate (1 C) was measured, and efficiency was always found to be nearly 100%. A comparative data (Table 1) is shown below where this work is compared with other contemporary V_2O_5 nanocomposite as cathode materials. The proposed material was obtained through a scalable synthesis process which shows high specific capacity, good cyclability, and enhanced rate capability when compared with similar materials as shown in the table.

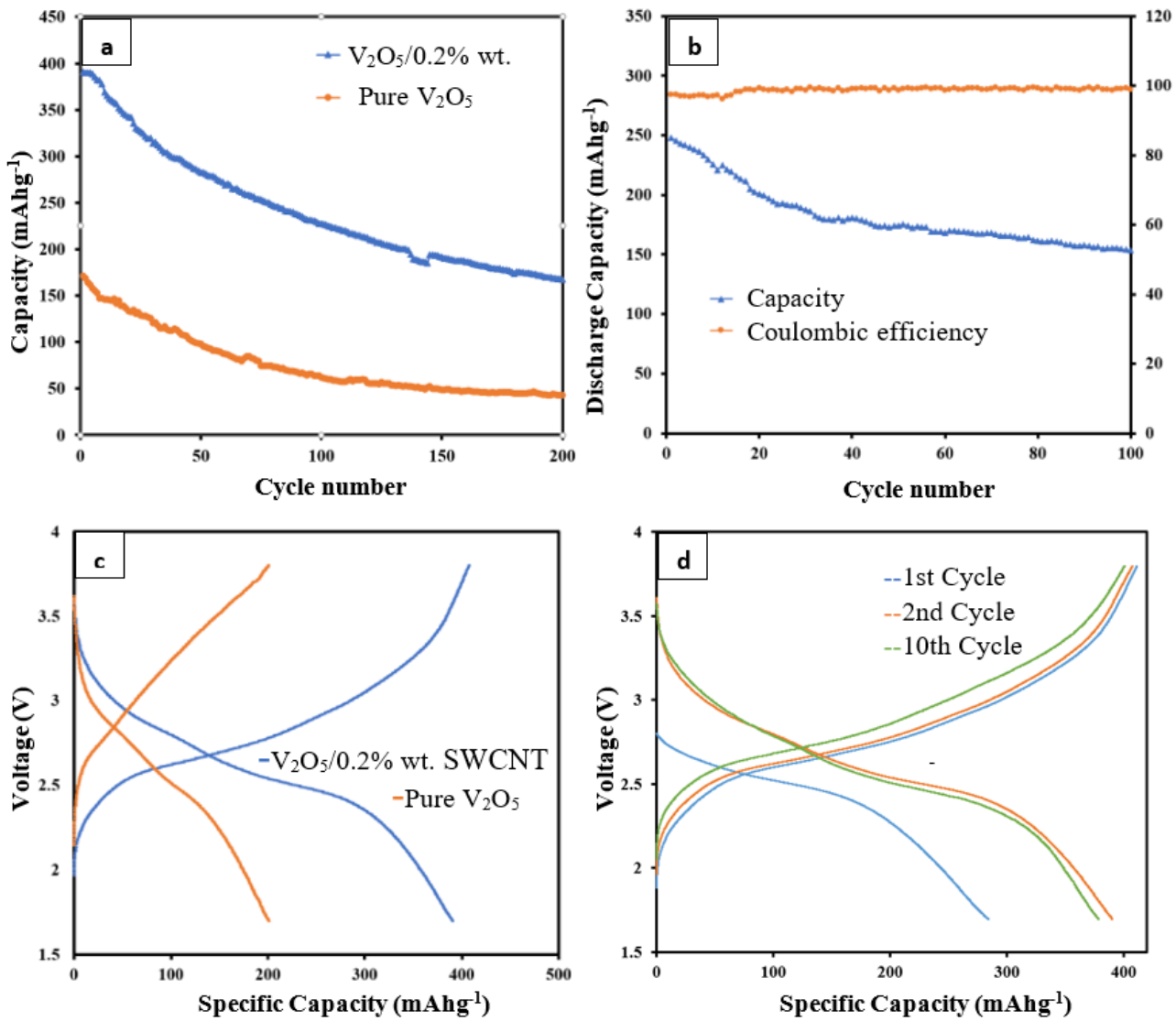

Figure 7. Electrochemical properties analysis. (**a**) Specific capacity of V_2O_5-SWCNT and pure V_2O_5 at a 0.1 C rate. (**b**) Cycle life with coulombic efficiency of V_2O_5-SWCNT at a 1 C rate. (**c**) Charge vs. discharge curves of coin cells made of pristine V_2O_5 and V_2O_5–SWCNT, respectively. (**d**) Charge–discharge curves of V_2O_5-SWCNT cells at 0.1 C rate for 1st, 2nd and 10th cycle.

Table 1. Comparison of our work and recently published works on V_2O_5/Carbon composites for lithium-ion batteries.

Materials	Morphology	Synthesis Method	Specific Capacity ($mAhg^{-1}$)	Cycle	Capacity Loss/Cycle	Current Density (mAg^{-1}) or C-Rate	Refs.
V_2O_5–C	Carbon-coated nanoparticles	RAPET dissociation	270	50	0.6	1 C	[55]
V_2O_5–CNTs	Interpenetrative nanocomposites of nanowires and CNTs	Hydrothermal reaction and subsequent filtration	340	50	0.48	0.25 C	[56]
V_2O_5–MWCNTs	Solid porous hybrid monolith	Controlled bubbling process	250	30	0.333	30	[57]
V_2O_5-MWCNTs	Nanocomposite structure	one-step solvothermal approach	265	100	0.75	1 C	[58]
V_2O_5–GO	Ultrathin nanowire attached on GO	Hydrothermal reaction and vacuum filtration method	294	200	0.05	100	[59]
V_2O_5–rGO	Porous polycrystalline nanospheres supported by rGO	Solvothermal treatment	238	50	0.3	90	[60]
V_2O_5-SWCNT	Sandwich structured V_2O_5/SWCNT	Facile sol–gel process followed by thermal treatment	390	200	0.3	0.1 C	This work

In terms of high-rate performance, the V_2O_5-SWCNT composite shows excellent properties compared to pure V_2O_5. At relatively higher current densities, the V_2O_5-SWCNT composite maintains far higher specific energy (375 $mAhg^{-1}$ at 0.5 C, 248 $mAhg^{-1}$ at 1 C, 225 $mAhg^{-1}$ at 3 C, 191 $mAhg^{-1}$ at 5 C, 158 $mAhg^{-1}$ at 10 C) compared to pure V_2O_5 (121 $mAhg^{-1}$ at 0.5 C, 110 $mAhg^{-1}$ at 1 C, 85 $mAhg^{-1}$ at 3 C, 61 $mAhg^{-1}$ at 5 C, 39 $mAhg^{-1}$ at 10 C) as shown in Figure 8a. These measurements correspond to an increase of 209%, 125%, 164%, 213% and 305% at the different C rates that were compared. After rates higher than 5 C, the specific capacity degradation is almost linear, where the lower C rate anomaly specific energy is recorded for both V_2O_5-SWCNT and V_2O_5 nanoparticles. At higher rates, performance data show that both electric conductivity and ionic conductivity increase in the V_2O_5-SWCNT composite. This is further supported by the alternating current (AC) impedance data which is discussed in detail later. The amount of SWCNT content in V_2O_5 xerogel plays a vital role and it was optimized separately by adding 0.05, 0.1, 0.2, 0.3, 0.5, 1.0 wt.% of SWCNT in V_2O_5. The specific capacity at 0.1 C for 0.05 wt.% of SWCNT is almost similar to pristine V_2O_5, whereas 0.1 wt.% shows a little increment in discharge capacity. In addition, 0.3 and 0.5 wt% SWCNT in V_2O_5 shows 370.5 and 356.2 $mAhg^{-1}$, respectively, with almost similar cycle stability of 0.2 wt.% SWCNT in V_2O_5. Furthermore, 1 wt.% SWCNT in V_2O_5 shows a sharp drop in specific capacity (250 $mAhg^{-1}$) but much improved cycle stability. A low amount of carbon nanotubes can be dispersed easily in V_2O_5 hydrogel, but a higher amount of carbon nanotubes starts restacking and blocking the V_2O_5 nanoribbons, which results in poor specific capacity.

Improved cycling stability was also observed for V_2O_5-SWCNT compared to pure V_2O_5. At a lower rate (0.1 C), we see that a specific capacity of 227 $mAhg^{-1}$ can be achieved after 100 cycles, which is around 60% of its primary capacity with the same current density. In the case of pure V_2O_5, after 100 cycles at 0.1 C, the capacity degrades to 62 $mAhg^{-1}$, only 37% of its initial capacity (168 $mAhg^{-1}$). The capacity decay rate in V_2O_5-SWCNT is only 0.4% where it is as high as 0.63% in pure V_2O_5. This indicates that the V_2O_5-SWCNT composite has a more stable structure. Higher SWCNT loading (0.5, 1, 2, 5%) into the V_2O_5

matrix was also explored. While increased loading provides less specific capacity than the 0.2% loading, all composites showed the same cycle stability. The data collected suggest that 0.2% loading leads to proper SWCNT distribution among V_2O_5 layers. It is theorized that higher loadings of SWCNT result in restacking with complete coverage over V_2O_5 nanoribbons, which ultimately hampers overall performance.

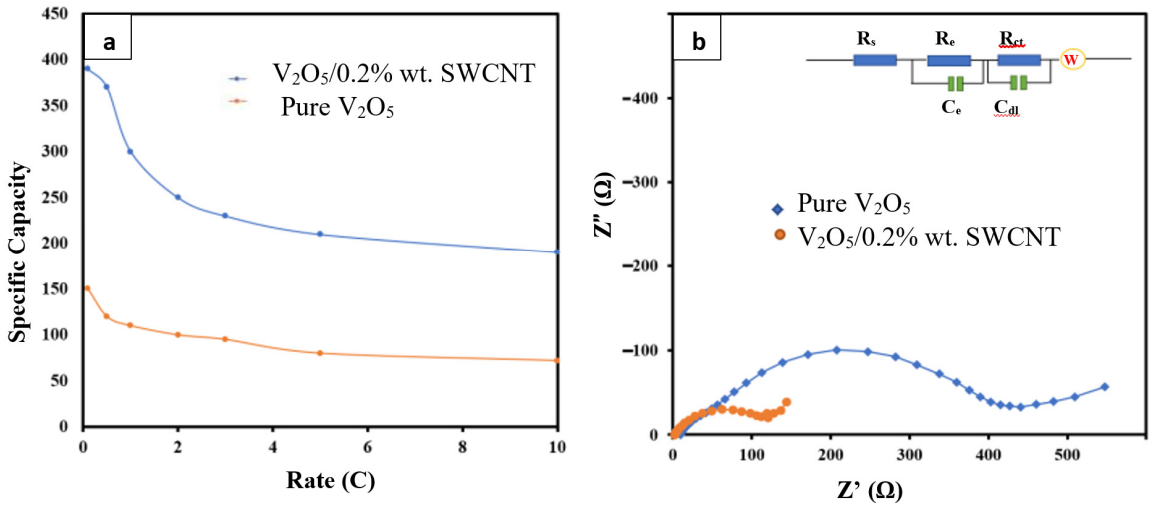

Figure 8. Rate performance comparison and Nyquist plot. (**a**) Rate performance of cells at different C-rate. (**b**) Nyquist plot of pristine V_2O_5 and V_2O_5/0.2% wt. SWCNT cells; amplitude: 5 mV; frequency:0.01 Hz-1 MHz.

AC impedance spectra was measured to validate the hypothesis that SWCNT insertion in between the bilayered structure of V_2O_5 leads to significantly improved Li+ ion intercalation, structural stability, electronic and ionic conductivity. Results obtained using the model are presented in Figure 8b (Nyquist plot) and show a substantial improvement in electronic conductivity. This was observed since the internal resistance (R_e) for V_2O_5-SWCNT composite had dropped from 414.80 to 120.74 ohm. Similar results have been found previously, when V_2O_5 was doped with Cu [61]. Importantly, pure V_2O_5 and V_2O_5-SWCNT composites were synthesized using the same process, with the only difference being the addition of SWCNTs.

This study has demonstrated how V_2O_5 coated with SWCNTs creates hybrid cathode materials for high performance batteries. The anchoring of V_2O_5 to the CNT surface is attained by a simple method as shown schematically in Figure 2. The ribbon-like structure of the V_2O_5 xerogels offers more exposure for Li^+ ion insertion into it than the crystalline-structured one. This provides more adaptable hosts for intercalating Li^+ ions, thereby demonstrating an improved potential for the lithium. Compared with conventional crystalline V_2O_5 and amorphous V_2O_5 xerogel, the V_2O_5-SWCNT hybrid xerogel offers further advantages due to its morphology. The fundamental unit of the V_2O_5 xerogel consists of two similar sheets with vanadium oxide layers. When the interspacing of adjoining layers increases, the intercalation capacity becomes higher. Subsequently, water molecules act as supports between vanadium oxide layers in a hydrated V_2O_5 xerogel, which is V_2O_5.nH2O, and they endorse a basal spacing of B11.5 Å [62]. This spacing leads to improved lithium-ion intercalation, which is measured as 1.4 times greater than orthorhombic structure of V_2O_5, (B4.56 Å). Furthermore, the greater interlayer distance promotes Li^+ diffusion in the V_2O_5 matrix. The interlayered molecules reside in a twisted pyramid–square ligand region that favors electron transmission and intercalation of Li^+ ions inside the V_2O_5 matrix. Nonetheless, the same difficulties of poor electrical conductivity (both intraparticles inside a V_2O_5 particle and interparticles among V_2O_5 particles) still exist for V_2O_5 xerogels, namely sluggish Li^+ diffusion and structural steadiness/reversibility problems. Our comprehensive approach addresses these issues by inserting a small (0.2%) amount of SWCNTs

between the V_2O_5 nanoribbons during the sol–gel process. The resultant arrangement increases electrical conduction of intraparticles and diffusion of lithium ions. In addition, the resultant smaller grain size of V_2O_5 in the V_2O_5 xerogel reduces stress between particles, leading to better structural stability and longer cycle life. In summary, here, we present an easy and novel synthesis approach of nanostructured V_2O_5-SWCNTs materials through the sol–gel method, resulting in a class of V_2O_5 hybrids with low intercalated carbon nanotubes concentrations (0.2 wt.%). These V_2O_5-SWCNTs hybrids resolve the challenges that plague other V_2O_5 xerogels and exhibit extraordinary electrochemical performance as a cathode material in practical lithium-ion battery applications.

6. Conclusions

In this work, the synthesis of V_2O_5-SWCNT nanocomposites using a simple sol–gel technique was presented. This process builds a V_2O_5 framework that entraps SWCNT layers to create a super conductive network with low resistivity. Morphology characterization shows a layered structure of V_2O_5 that can be modified by a hydrothermal technique that allows nanoparticles to be inserted between layers. This is shown to significantly improve the electrochemical properties of V_2O_5, making a material that is superior for cathode applications in lithium-ion batteries. Other systematic electrochemical testing was used to justify the claim that well-processed V_2O_5 with a small amount of SWCNT (0.2–0.5%) can bring a large change in surface area in order to yield an ultrahigh specific capacity: 390 $mAhg^{-1}$ (88% of the theoretical capacity: 443 $mAhg^{-1}$), super cyclability (degradation only about 0.3% per cycle during 200 cycles), high-rate capability, and above all, outstanding Li-ion storage and conversion behavior. The large conductive network of the V_2O_5-SWCNT composite effectively buffers against cycling strain, alleviating low Li^+ diffusion and strain relaxation of the electrode. The presented work does not considerably increase the cost of cathode materials, as only small amounts of SWCNT are required to make large improvements. Currently, there is a global trend toward producing flexible lithium-ion batteries for electronics and structural batteries for automobile industries, but conventional cathode materials are inadequate to serve those purposes due to their poor electrochemical performance and high cost. As V_2O_5 is abundant in nature and the challenges of widespread industrial applications can be eliminated by introducing a small amount of nanofillers, i.e., CNTs, our novel V_2O_5-SWCNT composite holds promise for the mass production of lithium-ion battery cathode materials and opens new doors to further investigate new V_2O_5 hybrid nanomaterials in the future.

Supplementary Materials: The following supporting information can be downloaded at: https://www.mdpi.com/article/10.3390/en15020552/s1, Figure S1: (a) SWCNT: PSS solution after two weeks and distribution curve of Z-average value with standard deviation which reflects well dispersion of SWCNT in the solution after two weeks (b) Only SWCNT solution after two weeks and distribution curve of Z-average value with standard deviation which reflects phase separation with abrupt size starting from 600 to 2000 d.nm. Figure S2: XRD patterns of the 400 °C annealed pristine V_2O_5 and V_2O_5-SWCNT.

Author Contributions: N.A.: Conceptualization, Methodology, Writing—original draft. P.K.B.: Conceptualization, Methodology, Writing—original draft. H.D.: Supervision, Writing—review and editing, Project administration, Funding acquisition. M.A.: Supervision, Writing—review and editing, Project administration, Funding acquisition. All authors have read and agreed to the published version of the manuscript.

Funding: This research received no external funding.

Acknowledgments: We acknowledge the assistance of Yadong Liu, IUPUI for helping us throughout the project by providing materials and lab facilities. We also thank Dan Minnner (Integrated Nanosystems Development Institute) and Mark David Woollam (IUPUI) for the assistance with the editing of the manuscript.

Conflicts of Interest: The authors declare that they have no known competing financial interests or personal relationships that could have appeared to influence the work reported in this paper.

References

1. Aliahmad, N.; Liu, Y.; Xie, J.; Agarwal, M. V_2O_5/Graphene Hybrid Supported on Paper Current Collectors for Flexible Ultrahigh-Capacity Electrodes for Lithium-Ion Batteries. *ACS Appl. Mater. Interf.* **2018**, *10*, 16490–16499. [CrossRef] [PubMed]
2. Goodenough, J.B.; Park, K.-S. The Li-Ion Rechargeable Battery: A Perspective. *J. Am. Chem. Soc.* **2013**, *135*, 1167–1176. [CrossRef]
3. Wakihara, M. Recent developments in lithium ion batteries. *Mater. Sci. Eng. R: Rep.* **2001**, *33*, 109–134. [CrossRef]
4. Xu, C.; Weng, L.; Ji, L.; Zhou, J. An analytical model for the fracture behavior of the flexible lithium-ion batteries under bending deformation. *Eur. J. Mech. A/Solids* **2019**, *73*, 47–56. [CrossRef]
5. Cha, H.; Kim, J.; Lee, Y.; Cho, J.; Park, M. Issues and Challenges Facing Flexible Lithium-Ion Batteries for Practical Application. *Small* **2017**, *14*, e1702989. [CrossRef]
6. Zeng, L.; Qiu, L.; Cheng, H.-M. Towards the practical use of flexible lithium ion batteries. *Energy Storage Mater.* **2019**, *23*, 434–438. [CrossRef]
7. Bruce, P.G.; Scrosati, B.; Tarascon, J.-M. Nanomaterials for Rechargeable Lithium Batteries. *Angew. Chem. Int. Ed.* **2008**, *47*, 2930–2946. [CrossRef]
8. Armand, M.; Tarascon, J.-M. Building better batteries. *Nature* **2008**, *451*, 652–657. [CrossRef] [PubMed]
9. Jiang, C.; Hosono, E.; Zhou, H. Nanomaterials for lithium ion batteries. *Nano Today* **2006**, *1*, 28–33. [CrossRef]
10. Yaroslavtsev, A.B.; Kulova, T.; Skundin, A.M. Electrode nanomaterials for lithium-ion batteries. *Russ. Chem. Rev.* **2015**, *84*, 826–852. [CrossRef]
11. Liu, H.K.; Wang, G.X.; Guo, Z.; Wang, J.; Konstantinov, K.; Konstantinov, K. Nanomaterials for Lithium-ion Rechargeable Batteries. *J. Nanosci. Nanotechnol.* **2006**, *6*, 1–15. [CrossRef]
12. Huang, H.; Yin, S.-C.; Nazar, L.S. Approaching theoretical capacity of LiFePO4 at room temperature at high rates. *Electrochem. Solid-State Lett.* **2001**, *4*, A170–A172. [CrossRef]
13. Amine, K.; Belharouak, I.; Chen, Z.; Tran, T.; Yumoto, H.; Ota, N.; Myung, S.-T.; Sun, Y.-K. Nanostructured Anode Material for High-Power Battery System in Electric Vehicles. *Adv. Mater.* **2010**, *22*, 3052–3057. [CrossRef]
14. Levi, R.; Bar-Sadan, M.; Albu-Yaron, A.; Popovitz-Biro, R.; Houben, L.; Prior, Y.; Tenne, R. Stability Criteria of Fullerene-like Nanoparticles: Comparing V_2O_5 to Layered Metal Dichalcogenides and Dihalides. *Materials* **2010**, *3*, 4428–4445. [CrossRef]
15. Jiang, Q.; Du, K.; He, Y. A novel method for preparation of LiNi1/3Mn1/3Co1/3O2 cathode material for Li-ion batteries. *Electrochim. Acta* **2013**, *107*, 133–138. [CrossRef]
16. Zhang, W.-J. Structure and performance of LiFePO4 cathode materials: A review. *J. Power Sources* **2011**, *196*, 2962–2970. [CrossRef]
17. Zhu, L.; Bao, C.; Xie, L.; Yang, X.; Cao, X. Review of synthesis and structural optimization of LiNi1/3Co1/3Mn1/3O2 cathode materials for lithium-ion batteries applications. *J. Alloy. Compd.* **2020**, *831*, 154864. [CrossRef]
18. Yue, Y.; Liang, H. Micro- and Nano-Structured Vanadium Pentoxide (V_2O_5) for Electrodes of Lithium-Ion Batteries. *Adv. Energy Mater.* **2017**, *7*, 1602545. [CrossRef]
19. Kaper, H.; Willinger, M.-G.; Djerdj, I.; Gross, S.; Antonietti, M.; Smarsly, B.M. IL-assisted synthesis of V_2O_5 nanocomposites and VO2 nanosheets. *J. Mater. Chem.* **2008**, *18*, 5761–5769. [CrossRef]
20. De Juan-Corpuz, L.M.; Corpuz, R.D.; Somwangthanaroj, A.; Nguyen, M.T.; Yonezawa, T.; Ma, J.; Kheawhom, S. Binder-Free Centimeter-Long V_2O_5 Nanofibers on Carbon Cloth as Cathode Material for Zinc-Ion Batteries. *Energies* **2019**, *13*, 31. [CrossRef]
21. Beke, S. A review of the growth of V_2O_5 films from 1885 to 2010. *Thin Solid Films* **2011**, *519*, 1761–1771. [CrossRef]
22. Cheah, Y.L.; Gupta, N.; Pramana, S.S.; Aravindan, V.; Wee, G.; Srinivasan, M. Morphology, structure and electrochemical properties of single phase electrospun vanadium pentoxide nanofibers for lithium ion batteries. *J. Power Sources* **2011**, *196*, 6465–6472. [CrossRef]
23. Delmas, C.; Cognac-Auradou, H.; Cocciantelli, J.; Ménétrier, M.; Doumerc, J. The LixV_2O_5 system: An overview of the structure modifications induced by the lithium intercalation. *Solid State Ionics* **1994**, *69*, 257–264. [CrossRef]
24. McColl, K.; Cora, F. Phase stability of intercalated V_2O_5 battery cathodes elucidated through the Goldschmidt tolerance factor. *Phys. Chem. Chem. Phys.* **2019**, *21*, 7732–7744. [CrossRef] [PubMed]
25. Liu, Q.; Li, Z.-F.; Liu, Y.; Zhang, H.; Ren, Y.; Sun, C.-J.; Lu, W.; Zhou, Y.; Stanciu, L.; Stach, E.A.; et al. Graphene-modified nanostructured vanadium pentoxide hybrids with extraordinary electrochemical performance for Li-ion batteries. *Nat. Commun.* **2015**, *6*, 6127. [CrossRef] [PubMed]
26. Zhang, X.; Wang, J.-G.; Liu, H.; Liu, H.; Wei, B. Facile Synthesis of V_2O_5 Hollow Spheres as Advanced Cathodes for High-Performance Lithium-Ion Batteries. *Materials* **2017**, *10*, 77. [CrossRef]
27. Cao, A.-M.; Hu, J.-S.; Liang, H.-P.; Wan, L.-J. Self-Assembled Vanadium Pentoxide (V_2O_5) Hollow Microspheres from Nanorods and Their Application in Lithium-Ion Batteries. *Angew. Chem. Int. Ed.* **2005**, *44*, 4391–4395. [CrossRef]
28. Ng, S.; Chew, S.; Wang, J.; Wexler, D.; Tournayre, Y.; Konstantinov, K.; Liu, H. Synthesis and electrochemical properties of V_2O_5 nanostructures prepared via a precipitation process for lithium-ion battery cathodes. *J. Power Sources* **2007**, *174*, 1032–1035. [CrossRef]
29. Liu, X.; Zeng, J.; Yang, H.; Zhou, K.; Pan, D. V_2O_5-Based nanomaterials: Synthesis and their applications. *RSC Adv.* **2018**, *8*, 4014–4031. [CrossRef]
30. Qian, Y.; Vu, A.; Smyrl, W.H.; Stein, A. Facile Preparation and Electrochemical Properties of V_2O_5-Graphene Composite Films as Free-Standing Cathodes for Rechargeable Lithium Batteries. *J. Electrochem. Soc.* **2012**, *159*, A1135–A1140. [CrossRef]

31. Chen, D.; Yi, R.; Chen, S.; Xu, T.; Gordin, M.L.; Lv, D.; Wang, D. Solvothermal synthesis of V_2O_5/graphene nanocomposites for high performance lithium ion batteries. *Mater. Sci. Eng. B* **2014**, *185*, 7–12. [CrossRef]
32. Ji, L.; Lin, Z.; Alcoutlabi, M.; Zhang, X. Recent developments in nanostructured anode materials for rechargeable lithium-ion batteries. *Energy Environ. Sci.* **2011**, *4*, 2682–2699. [CrossRef]
33. Kim, S.-H.; Choi, K.-H.; Cho, S.-J.; Choi, S.; Park, S.; Lee, S.-Y. Printable Solid-State Lithium-Ion Batteries: A New Route toward Shape-Conformable Power Sources with Aesthetic Versatility for Flexible Electronics. *Nano Lett.* **2015**, *15*, 5168–5177. [CrossRef]
34. Wen, L.; Li, F.; Cheng, H.-M. Carbon Nanotubes and Graphene for Flexible Electrochemical Energy Storage: From Materials to Devices. *Adv. Mater.* **2016**, *28*, 4306–4337. [CrossRef] [PubMed]
35. Alawi, O.A.; Mallah, A.R.; Kazi, S.N.; Sidik, N.A.C.; Najafi, G. Thermophysical properties and stability of carbon nanostructures and metallic oxides nanofluids. *J. Therm. Anal. Calorim.* **2018**, *135*, 1545–1562. [CrossRef]
36. Lim, A.; Lam, Y. Numerical Investigation of Nanostructure Orientation on Electroosmotic Flow. *Micromachines* **2020**, *11*, 971. [CrossRef] [PubMed]
37. Ladpli, P.; Nardari, R.; Kopsaftopoulos, F.; Chang, F.-K. Multifunctional energy storage composite structures with embedded lithium-ion batteries. *J. Power Sources* **2019**, *414*, 517–529. [CrossRef]
38. Biswas, P.K.; Aliahmad, N.; Dalir, H.; Agarwal, M. Nanostructured V_2O_5-SWCNTs based lithium ion battery for multifunctional energy storage composites: Materials synthesis and fabrication. *AIAA Scitech 2021 Forum* **2021**, 1006. [CrossRef]
39. Lee, C.Y.; Marschilok, A.C.; Subramanian, A.; Takeuchi, K.J.; Takeuchi, E.S. Synthesis and characterization of sodium vanadium oxide gels: The effects of water (n) and sodium (x) content on the electrochemistry of Na(x)V_2O_5.nH2O. *Phys. Chem. Chem. Phys.* **2011**, *13*, 18047–18154. [CrossRef]
40. Meyer, C.; Bockholt, H.; Haselrieder, W.; Kwade, A. Characterization of the calendering process for compaction of electrodes for lithium-ion batteries. *J. Mater. Process. Technol.* **2017**, *249*, 172–178. [CrossRef]
41. Livage, J. Hydrothermal Synthesis of Nanostructured Vanadium Oxides. *Materials* **2010**, *3*, 4175–4195. [CrossRef]
42. Xu, F.; Zhang, H.; Ilavsky, J.; Stanciu, L.; Ho, D.; Justice, M.J.; Petrache, H.I.; Xie, J. Investigation of a Catalyst Ink Dispersion Using Both Ultra-Small-Angle X-ray Scattering and Cryogenic TEM. *Langmuir* **2010**, *26*, 19199–19208. [CrossRef] [PubMed]
43. Lee, K.; Lim, H.J.; Yang, S.J.; Kim, Y.S.; Park, C.R. Determination of solubility parameters of single-walled and double-walled carbon nanotubes using a finite-length model. *RSC Adv.* **2013**, *3*, 4814–4820. [CrossRef]
44. Davis, V.; Parra-Vasquez, A.N.G.; Green, M.; Rai, P.K.; Behabtu, N.; Prieto, V.; Booker, R.D.; Schmidt, J.; Kesselman, E.; Zhou, W.; et al. True solutions of single-walled carbon nanotubes for assembly into macroscopic materials. *Nat. Nanotechnol.* **2009**, *4*, 830–834. [CrossRef] [PubMed]
45. Wei, L.; Zhang, Y. Covalent sidewall functionalization of single-walled carbon nanotubes via one-electron reduction of benzophenone by potassium. *Chem. Phys. Lett.* **2007**, *446*, 142–144. [CrossRef]
46. Beesley, D.J.; Price, B.K.; Hunter, S.; Shaffer, M.S.P.; de Mello, J.C. Direct dispersion of SWNTs in highly conductive solvent-enhanced PEDOT:PSS films. *Nanocomposites* **2016**, *2*, 135–140. [CrossRef]
47. Li, H.; Adronov, A. Water-soluble SWCNTs from sulfonation of nanotube-bound polystyrene. *Carbon* **2007**, *45*, 984–990. [CrossRef]
48. Jiang, H.; Wei, Z.; Cai, X.; Lai, L.; Ma, J.; Huang, W. A cathode for Li-ion batteries made of vanadium oxide on vertically aligned carbon nanotube arrays/graphene foam. *Chem. Eng. J.* **2018**, *359*, 1668–1676. [CrossRef]
49. Cao, Z.; Wei, B. V_2O_5/single-walled carbon nanotube hybrid mesoporous films as cathodes with high-rate capacities for rechargeable lithium ion batteries. *Nano Energy* **2013**, *2*, 481–490. [CrossRef]
50. Sathiya, M.; Prakash, A.S.; Ramesha, K.; Tarascon, J.; Shukla, A.K. V_2O_5-Anchored Carbon Nanotubes for Enhanced Electrochemical Energy Storage. *J. Am. Chem. Soc.* **2011**, *133*, 16291–16299. [CrossRef] [PubMed]
51. Daneshkhah, A.; Vij, S.; Siegel, A.; Agarwal, M. Polyetherimide/carbon black composite sensors demonstrate selective detection of medium-chain aldehydes including nonanal. *Chem. Eng. J.* **2019**, *383*, 123104. [CrossRef]
52. McCafferty, E.; Wightman, J.P. Determination of the concentration of surface hydroxyl groups on metal oxide films by a quantitative XPS method. *Surf. Interface Anal.* **1998**, *26*, 549–564. [CrossRef]
53. Hu, B.; Li, L.; Xiong, X.; Liu, L.; Huang, C.; Yu, D.; Chen, C. High-performance of copper-doped vanadium pentoxide porous thin films cathode for lithium-ion batteries. *J. Solid State Electrochem.* **2019**, *23*, 1315–1324. [CrossRef]
54. Livage, J. Synthesis of polyoxovanadates via "chimie douce". *Coord. Chem. Rev.* **1998**, *178–180*, 999–1018. [CrossRef]
55. Wang, J.; Curtis, C.J.; Schulz, D.L.; Zhang, J.-G. Influences of Treatment Temperature and Water Content on Capacity and Rechargeability of V_2O_5 Xerogel Films. *J. Electrochem. Soc.* **2004**, *151*, A1–A7. [CrossRef]
56. Odani, A.; Pol, V.G.; Pol, S.V.; Koltypin, M.; Gedanken, A.; Aurbach, D. Testing Carbon-Coated VOx Prepared via Reaction under Autogenic Pressure at Elevated Temperature as Li-Insertion Materials. *Adv. Mater.* **2006**, *18*, 1431–1436. [CrossRef]
57. Jia, X.; Chen, Z.; Suwarnasarn, A.; Rice, L.; Wang, X.; Sohn, H.; Zhang, Q.; Wu, B.M.; Wei, F.; Lu, Y. High-performance flexible lithium-ion electrodes based on robust network architecture. *Energy Environ. Sci.* **2012**, *5*, 6845–6849. [CrossRef]
58. Carn, F.; Morcrette, M.; Desport, B.; Backov, R. Lithium-ion battery electrode prepared by confining carbon nanotubes/V_2O_5 nanoribbons suspension in model air–liquid foams. *Solid State Sci.* **2013**, *17*, 134–139. [CrossRef]
59. Partheeban, T.; Kesavan, T.; Vivekanantha, M.; Sasidharan, M. One-pot solvothermal synthesis of V_2O_5/MWCNT composite cathode for Li ion batteries. *Appl. Surf. Sci.* **2019**, *493*, 1106–1114. [CrossRef]
60. Lee, J.W.; Lim, S.Y.; Jeong, H.M.; Hwang, T.H.; Kang, J.K.; Choi, J.W. Extremely stable cycling of ultra-thin V_2O_5 nanowire–graphene electrodes for lithium rechargeable battery cathodes. *Energy Environ. Sci.* **2012**, *5*, 9889–9894. [CrossRef]

61. Wei, Y.; Ryu, C.-W.; Kim, K.-B. Improvement in electrochemical performance of V_2O_5 by Cu doping. *J. Power Sources* **2007**, *165*, 386–392. [CrossRef]
62. Rui, X.; Zhu, J.; Sim, D.; Xu, C.; Zeng, Y.; Hng, H.H.; Lim, T.M.; Yan, Q. Reduced graphene oxide supported highly porous V_2O_5 spheres as a high-power cathode material for lithium ion batteries. *Nanoscale* **2011**, *3*, 4752–4758. [CrossRef] [PubMed]